Neurobiology of Aging 75 (2019) 83–97

Contents lists available at ScienceDirect

Neurobiology of Aging

journal homepage: www.elsevier.com/locate/neuaging

Iron-related nigral degeneration influences functional topology mediated by striatal dysfunction in Parkinson's disease

Xiaojun Guan [a,b], Yuyao Zhang [b], Hongjiang Wei [b], Tao Guo [a], Qiaoling Zeng [a], Cheng Zhou [a], Jiaqiu Wang [c], Ting Gao [c], Min Xuan [a], Quanquan Gu [a], Xiaojun Xu [a], Peiyu Huang [a], Jiali Pu [c], Baorong Zhang [c], Chunlei Liu [b,d,**], Minming Zhang [a,*]

[a] Department of Radiology, The Second Affiliated Hospital, Zhejiang University School of Medicine, Hangzhou, China
[b] Department of Electrical Engineering and Computer Sciences, University of California, Berkeley, CA, USA
[c] Department of Neurology, The Second Affiliated Hospital, Zhejiang University School of Medicine, Hangzhou, China
[d] Helen Wills Neuroscience Institute, University of California, Berkeley, CA, USA

ARTICLE INFO

Article history:
Received 13 July 2018
Received in revised form 12 November 2018
Accepted 13 November 2018
Available online 22 November 2018

Keywords:
Parkinson's disease
Iron
Quantitative susceptibility mapping
Diffusion tensor imaging
Functional magnetic resonance imaging

ABSTRACT

In Parkinson's disease (PD), iron accumulation in the substantia nigra (SN) exacerbates oxidative stress and α-synuclein aggregation, leading to neuronal death. However, the influence of iron-related nigral degeneration on the subcortical function and global network configuration in PD remains unknown. Ninety PD patients and 38 normal controls underwent clinical assessments and multimodality magnetic resonance imaging scans. Iron accumulation in the inferior SN and disrupted functional connectivity between the bilateral striatums were observed in PD, and negative correlation between them was found in the whole population. The binarized functional network exhibited enhanced global efficiency and reduced local efficiency while the weighted functional network exhibited reduction in both, and both changes were correlated with nigral iron accumulation in PD. Mediation analysis demonstrated that the functional connectivity between bilateral striatums was a mediator between the nigral iron accumulation and weighted functional network alterations. In conclusion, our findings reveal that iron-related nigral degeneration possibly influences the functional topology mediated by striatal dysfunction, which extends the scientific understanding of PD pathogenesis.

1. Introduction

Parkinson's disease (PD) is one of the most common movement disorders (Lees et al., 2009) and is pathologically characterized by the aberrant accumulation of α-synuclein and loss of dopaminergic neurons in the substantia nigra (SN) pars compacta (SNc) (Braak et al., 2003; Spillantini et al., 1997). Although the exact pathogenesis of PD is not fully understood, a large amount of histochemical evidence (Dexter et al., 1991; Jellinger et al., 1990; Sofic et al., 1991) suggests that excessive iron overload in the SN is a potential cause for the death of dopaminergic neurons. Pathologically, iron accumulation in the SN can induce irreversibly neurodegenerative processes through mechanisms including oxidative reaction and neurotoxicity (Jellinger, 1999; Ward et al., 2014). Given that the expression of α-synuclein is modified by iron in vitro, nigral iron accumulation could result in the aggregation of α-synuclein thus blooming its toxicity (Ostrerova-Golts et al., 2000; Wan et al., 2017). It is already known that the iron distribution within the SN is spatially inhomogeneous (Lotfipour et al., 2012; Massey et al., 2017), but whether pathological iron accumulation occurs in a specific SN subregion is not fully known in PD (Du et al., 2012; Lotfipour et al., 2012). Therefore, quantitative exploration of nigral iron in specific subregions has the potential to extend our understanding of iron-related pathogenesis in PD.

PD-related pathogenesis involves not only the SN but also other brain regions. Owing to the nigral degeneration, the secondary depletion of dopamine, a major afferent neurotransmitter to striatum (Kish et al., 1988), could widely disturb the functions of basal ganglia and the cortex connected to it (Guan et al., 2017a; Obeso et al., 2000; Szewczyk-Krolikowski et al., 2014) and contribute to connectivity impairments in multiple cerebral networks (Bell et al., 2015; Shine et al., 2013a,b). Furthermore, prion-like spread of toxic α-synuclein stemming from the brainstem to neocortex is observed

* Corresponding author at: Department of Radiology, The Second Affiliated Hospital, Zhejiang University School of Medicine, No.88 Jiefang Road, Shangcheng District, Hangzhou, China, 31009. Tel.: 86-0571-87315255; fax: 86-0571-8735255.
** Corresponding author at: Department of Electrical Engineering and Computer Sciences, and The Helen Wills Neuroscience Institute at the University of California, Berkeley, 505 Cory Hall, Berkeley, CA 94720, USA. Tel.: 1-510-6647596; fax: 1-510-6437846.
E-mail addresses: chunlei.liu@berkeley.edu (C. Liu), zhangminming@zju.edu.cn (M. Zhang).

0197-4580/$ – see front matter © 2018 Elsevier Inc. All rights reserved.
https://doi.org/10.1016/j.neurobiolaging.2018.11.013

in symptomatic PD patients (Braak et al., 2003; Jucker and Walker, 2013). Thus, it is possible that the global network of PD could be perturbed under this pathological stress, where striatal function may play an important intermediate role. However, although the neurotoxicity of iron accumulation in dopaminergic neurons is well documented (Jellinger, 1999; Ward et al., 2014), in vivo evidence relating to the effects of iron-related nigral degeneration on the striatal function and global network configuration is lacking.

To address this question, we used multimodality magnetic resonance imaging (MRI) data, including quantitative susceptibility mapping (QSM), resting-state functional MRI (rsfMRI), and diffusion tensor imaging (DTI), to investigate subregion-specific nigral iron accumulation and its correlations with the altered subcortical connectivity and global network topology. Compared with previous MRI technologies (e.g., R2* mapping), QSM provides high sensitivity to brain iron and allows for localized iron quantification by removing the susceptibility effect from surrounding tissue (Bilgic et al., 2012; Langkammer et al., 2012; Liu et al., 2015; Wang and Liu, 2015), and it has been shown to reflect the iron-related nigral degeneration in PD (Du et al., 2016; Guan et al., 2017b; He et al., 2015; Langkammer et al., 2016). To measure the typical dysfunction of the basal ganglia regions in PD (Guan et al., 2017a; Obeso et al., 2000; Szewczyk-Krolikowski et al., 2014), seed-based resting-state functional connectivity among the striatum, pallidum, and thalamus was used. Graph theory–based network analysis, constructed from functional and diffusional data, enables the estimations of information segregation and integration both functionally and structurally (Gong et al., 2009; Liao et al., 2017; Sporns et al., 2005), which is potentially useful for examining the biological mechanisms of PD (Abbasi et al., 2018; Berman et al., 2016; Galantucci et al., 2017; Luo et al., 2015; Skidmore et al., 2011; Suo et al., 2017; Wen et al., 2017). Using these neuroimaging methods, we evaluated the hypothesis that iron accumulation in certain nigral subregions might impart perturbations to functional and/or structural network topology mediated by striatal dysfunction.

2. Materials and methods

2.1. Subjects

All patients with PD and normal controls signed informed consent forms in accordance with the approval of the Medical Ethic Committee of the Second Affiliated Hospital of Zhejiang University School of Medicine.

The diagnosis of PD was made by a senior neurologist (BZ) according to the United Kingdom PD Society Brain Bank criteria (Hughes et al., 1992). Initially, a total of 151 patients who underwent enhanced susceptibility-weighted angiography (ESWAN) scanning were recruited from August 2014 to August 2017. For patients with PD who were under antiparkinsonian treatment, clinical assessments and MRI scanning were performed in the morning after withdrawing all antiparkinsonian drugs overnight (at least 12 hours) (on “drug-off status”). Basic demographic information, such as age, gender, education, and disease duration, and neurologic and psychiatric scales including Unified Parkinson’s Disease Rating Scale (UPDRS), Hoehn-Yahr stage, the Mini–Mental State Examination (MMSE) score, and the Parkinson’s Disease Questionnaire (39 questions) (PDQ-39) were obtained from all patients. The PDQ-39 is a quality-of-life measure that consists of 39 items in which patients use a scale 0-4 to rate how often they have experienced PD-related symptoms and difficulties over the last month where higher scores indicate greater symptom severity (Den Oudsten et al., 2007; Peto et al., 1995). For normal controls, basic demographic information, UPDRS motor scale, and MMSE score were recorded.

Participants with a history of neurologic or psychiatric disorders, brain trauma, or general exclusion criteria for MR scanning and analyzing were excluded from the study. Specifically, for iron quantification, 4 normal controls and 19 patients with PD were excluded for the following reasons: (1) with potentially cognitive impairment according to MMSE estimated by the criteria suitable for Chinese population (MMSE score $\leq$ 17 for illiterate, $\leq$ 20 for grade-school literate, and $\leq$ 23 for junior high school and higher education literate) (Guan et al., 2017a; Katzman et al., 1988; Zhang et al., 1990), n = 5; (2) with significant motion artifact during scanning, n = 8; (3) with severe brain atrophy or enlarged ventricles, n = 3; (4) with other neurologic or psychiatric disease history, n = 4; (5) with incomplete demographic information, n = 1; and (6) with poor coregistration results, n = 2. After exclusion, 90 patients with PD and 38 normal controls were included in the present study.

For resting-state functional network calculation, 121 of 128 participants were included (86 PD patients and 35 normal controls) because 3 participants’ data had more than 1/3 time points removed after scrubbing and 4 participants did not have rsfMRI data. For structural network construction, 121 of 128 participants were included (84 PD patients and 37 normal controls) because 7 participants did not have DTI data.

2.2. MRI scanning

All participants were scanned on a 3.0-Tesla MRI scanner (GE Discovery 750) equipped with an 8-channel head coil. During MRI scanning, the head was stabilized using restraining foam pads, and earplugs were provided to reduce the noise during scanning. Structural T1 images were acquired using a fast spoiled gradient recalled sequence: repetition time = 7.336 ms; echo time = 3.036 ms; inversion time = 450 ms; flip angle = 11°; field of view = 260 × 260 mm^2; matrix = 256 × 256; slice thickness = 1.2 mm; 196 continuous sagittal slices. ESWAN images were acquired using gradient recalled echo sequence: repetition time = 33.7 ms; first echo time/spacing/eighth echo time = 4.556 ms/3.648 ms/30.092 ms; flip angle = 20°; field of view = 240 × 240 mm^2; matrix = 416 × 384; slice thickness = 2 mm; slice gap = 0 mm; 64 continuous axial slices. Resting-state fMRI images were acquired using gradient recalled echo-echo planar imaging sequence: repetition time = 2000 ms; echo time = 30 ms; flip angle = 77°; field of view = 240 × 240 mm^2; matrix = 64 × 64; slice thickness = 4 mm; slice gap = 0 mm; 38 interleaved axial slices. DTI images were scanned using gradient recalled echo-echo planar imaging sequence with 32 gradient directions (b value = 1000 s/m^2): repetition time = 8000 ms; echo time = 80 ms; flip angle = 90°; field of view = 256 × 256; matrix = 128 × 128; slice thickness = 2 mm; slice gap = 0 mm; 67 interleaved axial slices.

2.3. QSM data processing and normalization

Susceptibility Tensor Imaging Suite V3.0 software package (https://people.eecs.berkeley.edu/~chunlei.liu/software.html) was used to calculate the susceptibility maps from the phase images. Specifically, the raw phase was unwrapped using a Laplacian-based phase unwrapping (Li et al., 2014, 2015), and the normalized phase was calculated. The normalized background phase was removed using the spherical-mean-value filtering (V_SHARP) (Wu et al., 2012). QSM images were calculated using STAR-QSM (STreaking Artifact Reduction for QSM) method (Wei et al., 2015, 2017). The mean signal from each individual brain was used as susceptibility reference.

To avoid subjective bias by manual measurement, an age-specific (51–60 years old) QSM template was used (Zhang et al.,

2018) to normalize the SN structure and facilitate the automatic quantification of nigral magnetic susceptibility. All QSM images in the native space were aligned with this age-specific QSM template using linear and nonlinear coregistrations (Fig. 1). In case of any coregistration bias, we visually examined the resulting normalized QSM images from each subject. The midbrain SN in the QSM template was equally divided into superior, middle, and inferior parts and their averaged bilateral magnetic susceptibility from each part of the SN was calculated.

As reviewed previously (Guan et al., 2017c; Lotfipour et al., 2012), because of the limited resolution of the clinical MRI scanner, there were different definitions for SN substructures. For example, many studies defined the tier with low signal between iron rich (bright signal in QSM) red nucleus and SN (located in the ventrolateral to red nucleus) as SNc (Du et al., 2016; Guan et al., 2017b,d; Martin et al., 2008; Wang et al., 2013). Therefore, as a control, we equally segmented this predefined SNc into superior, middle, and inferior parts in the template space and the averaged bilateral magnetic susceptibility from each subregion of SNc was calculated (Fig. S1).

2.4. Resting-state fMRI preprocessing and functional network construction

The rsfMRI data preprocessing was performed using the standard pipeline in the Data Processing & Analysis for (Resting-State) Brain Imaging suite (http://rfmri.org/dpabi) (Yan et al., 2016), which included the following steps: removal of the first 10 volumes, slice timing, realignment, the regression of nuisance covariates (Friston 24 head motion parameters, white matter, and cerebrospinal fluid signal), spatial normalization through structure images, smoothing with a gaussian kernel of $6 \times 6 \times 6$ mm^3 full width at half maximum, temporal band-pass filtering (0.01–0.1 Hz), linear detrending, and scrubbing. No subject showed apparent head motion over 2 mm (transformation) and/or 2° (rotation) after excluding the participants mentioned previously according to the ESWAN criteria.

In the functional network, nodes represent defined brain regions and edges represent the interregional functional connectivity between each pair of nodes. The anatomical automatic labeling (AAL) atlas with 90 regions of interest was used to generate network nodes.

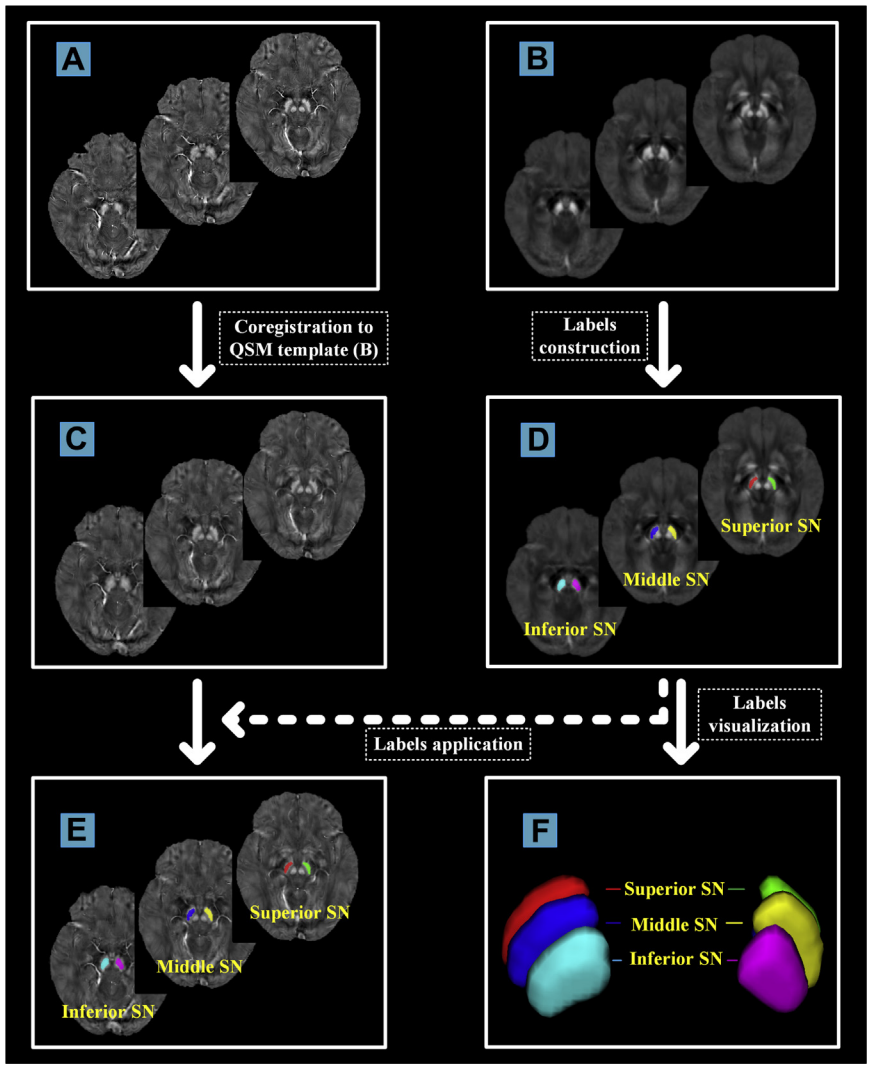

Fig. 1. The flowchart for automatic extraction of normalized nigral magnetic susceptibility. (A) QSM images in the native space; (B) age-specific QSM template generated from the ages range between 51 and 60 years; (C) normalized individual QSM images by linear and nonlinear coregistrations to the QSM template (B); (D) the labels of SN subregions manually drew in the QSM template; (E) the labels of SN subregions defined on the QSM template overlaid in the normalized individual QSM images; and (F) 3D visualization of manual segmentation of the SN in the template space. The identification of the predefined SNc and its 3D visualization were shown in the supplementary figure. Abbreviations: QSM, quantitative susceptibility mapping; SN, substantia nigra; SNc, SN pars compacta.

The mean time course of each node was extracted, and interregional resting-state functional connectivity was calculated based on the Pearson correlation between the time courses of each node pair (Figs. 2A and B). Fisher's r-to-z transformation was applied to improve data distributions for parametric statistical analysis.

The striatum, composed of caudate nucleus and putamen, is the main dopaminergic afference and is the mostly directly affected region after nigral degeneration (Kish et al., 1988). Therefore, functional connectivity among the striatum, pallidum, and thalamus was computed to explore the intrinsic subcortical rewiring.

2.5. DTI preprocessing and structural network construction

DTI images were preprocessed and structural network construction was performed by using the Pipeline for Analyzing braiN Diffusion imAges (PANDA) toolbox (http://www.nitrc.org/projects/panda/) (Cui et al., 2013), which is established on a few packages, e.g., FMRIB Diffusion Toolbox (http://www.fmrib.ox.ac.uk/fsl/) and Diffusion Toolkit software (http://trackvis.org/dtk/). The preprocessing procedure was composed of (1) skull stripping, (2) motion and eddy current correction, and (3) diffusion parameter calculation (i.e., fractional anisotropy [FA]). For each subject, whole-brain deterministic fiber tracking was conducted in the native diffusion space via the fiber assignment by the continuous tracking algorithm (Mori et al., 1999). Tractography was terminated if it turned at an angle $>45^\circ$ or reached a voxel with an FA < 0.2.

The DTI structural network used the same nodes as the functional network. For each participant, the parcellation process was conducted in the FA native space by following steps (Fig. 2C–I) (Gong et al., 2009; Zhong et al., 2017): (1) individual FA images were linearly coregistered to the T1-weighted images; (2) the T1-weighted images were then nonlinearly coregistered to the ICBM-152 template in the MNI space; (3) the AAL atlas from the MNI space was warped to the FA native space by applying the inverse transformation matrices; and (4) 90 cortical and subcortical nodes were generated by extracting the regions in the FA space. To determine the brain network edges, FA-weighted structural connectivity between each pair of nodes was used (Abbasi et al., 2018; Cui et al., 2013; Gong et al., 2009).

2.6. Global property calculation

Four global attributes of network topology defined by the Brain Connectivity Toolbox (Rubinov and Sporns, 2010) including global efficiency, local efficiency, characteristic path length, and clustering coefficient were computed for both functional and structural networks by using the GRETNA toolbox (http://www.nitrc.org/projects/gretna/) (Wang et al., 2015). Global efficiency indicates

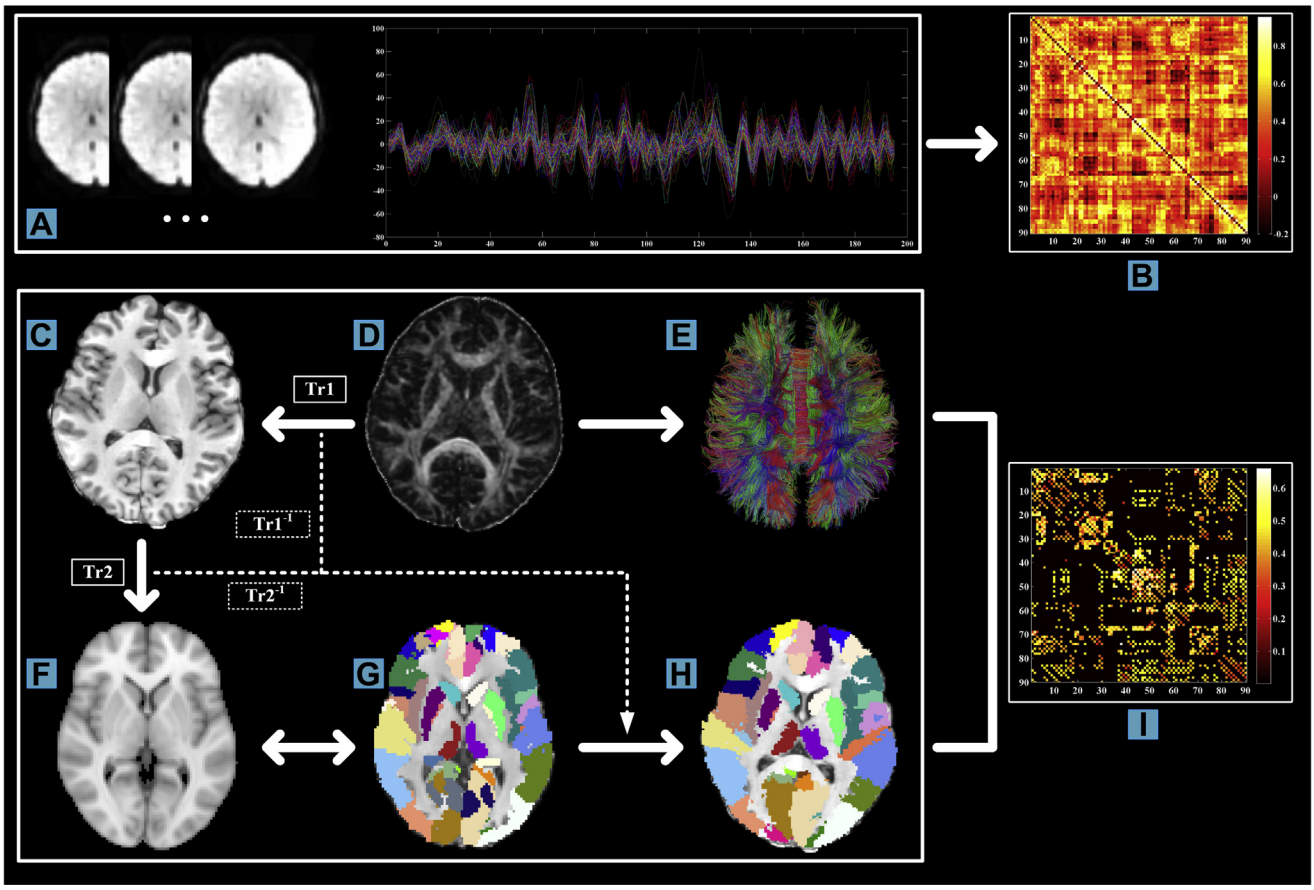

Fig. 2. The flowchart for network constructions on functional and diffusional data. (A) Regional time courses extracted based on AAL atlas (90 nodes); (B) the generated correlation matrix (90 × 90) of interregional functional connectivity; (C) T1-weighted images in the native space; (D) FA images in the native space; (E) deterministic tractography based on (D); (F) ICBM-152 T1 template in the MNI space; (G) AAL parcellation in the individual images in the MNI space; (H) AAL parcellation in the native space; and (I) the generated correlation matrix (90 × 90) of FA-weighted structural connectivity. Tr1: the transformation from FA images in the native space (subfigure D) to the T1-weighted images (subfigure C); Tr2: the transformation from the T1-weighted images (subfigure C) to the ICBM-152 T1 template in the MNI space (subfigure F). $Tr1^{-1}$ and $Tr2^{-1}$ denote the inverse transformation of Tr1 and Tr2, respectively, which were used to warp AAL parcellation from the MNI space to the native space. "↔" represented these images are in the same space (MNI space). Abbreviations: AAL, anatomical automatic labeling; FA, fractional anisotropy; MNI, Montreal Neurological Institute.

the efficiency of parallel information transfer in the whole network while local efficiency measures communication efficiency among the first neighbors of a given node when it is removed. Characteristic path length and clustering coefficient are 2 important attributes for the small-worldness of the human network (Liao et al., 2017; Rubinov and Sporns, 2010; Sporns et al., 2005). The human brain typically has small-worldness with short characteristic path length and large clustering coefficient, which supports integrated and specialized information processing with high efficiency (Liao et al., 2017; Rubinov and Sporns, 2010; Sporns et al., 2005; Watts and Strogatz, 1998).

In network calculation, as suggested by previous literature (Berman et al., 2016; Ginestet et al., 2011; Liao et al., 2017; Muldoon et al., 2016; Rubinov and Sporns, 2010), a binarized network where the connection between 2 nodes is either present or absent could be used to independently estimate network skeleton, whereas a weighted network that quantifies connection between each pair of nodes could reflect the topological connectivity. Therefore, graph attributes computed from both binarized and weighted networks could give complementary estimation of networks of the PD brain.

For the network property computation has a strong dependency on the network sparsity (Bullmore and Bassett, 2011), each correlation matrix was thresholded by applying a set of sparsity (Rubinov and Sporns, 2010). A fixed sparsity was computed as the ratio of the total number of existing edges with all possible total number of edges. Because the edge sparsity has no unified selection (Abbasi et al., 2018; Lu et al., 2017; Luo et al., 2015), in the present study, we repeatedly calculated the networks with a wide range of sparsity. A range of sparsity from 5% to 50% with an interval of 5% was selected for the functional networks and 10% to 30% with an interval of 2% was selected for the structural networks.

To investigate group differences in these networks, the area under the curve (AUC) for each global attribute was calculated, which provides a summarized scalar for topological characterization of the brain network (Lu et al., 2017; Luo et al., 2015).

2.7. Statistical analysis

The one-sample Kolmogorov-Smirnov test was used to check normality of the data. Differences in the age, education, UPDRS motor score, and gender distribution between groups were compared with the unpaired *t*-test, the Mann-Whitney *U* test, and the Pearson chi-squared test appropriately. To confirm the iron distribution within the SN and the predefined SNc, paired t-tests were conducted among 3 subregions of each. The intergroup comparisons of nigral magnetic susceptibility, AUC value from each global attribute, and subcortical functional connectivity were done using the general linear model. Partial correlation analyses were performed to detect the underlying relationships between the clinical scales and nigral magnetic susceptibility, the AUC values of global attributes, and the subcortical functional connectivity showing intergroup differences. To explore the relationships among nigral iron accumulation, altered subcortical functional connectivity, and global attributes, partial correlation analyses were conducted. As age and gender were well matched in the present study, to prevent overcorrection of age- and gender-related effects, in the above statistical analyses, we only regressed out the covariate of education, which had significant intergroup difference; $p < 0.05$ was generally considered as statistically significant. Bonferroni correction was used for intergroup comparisons of brain metrics. Specifically, for iron quantification in SN and SNc subregions, $p < 0.017$ (0.05/3) was regarded as significant, whereas for global attributes of functional networks, $p < 0.013$ (0.05/4) was regarded as significant. For the subcortical functional connectivity, $p < 0.003$ (0.05/15) was considered as significant. All of these analyses were performed by using IBM SPSS 19.0.

Based on the demonstrated associations among iron content in the inferior SN, striatal interconnectivity, and functional topological connectivity, we further conducted mediation analysis to test that whether striatal interconnectivity was a mediator between nigral iron accumulation (independent variable) and global perturbation of the functional network (outcome variable) for each group. A statistic toolbox (PROCESS Procedure for SPSS Release 2.16.3, http://www.afhayes.com/index.html) was used. Indirect effect of the iron accumulation in the inferior SN on the functional network through striatal interconnectivity was estimated by using bootstrapping approach with 1000 resampling (Preacher and Hayes, 2004). To derive the 95% confidence interval, the elements of the vector of 1000 estimates of indirect effect were sorted from low to high. In the sorted distribution of these estimates, the lower limit of the confidence interval is defined as the 25th estimate and the upper limit is defined as the 976th estimate. The outcome of indirect effect was considered as statistically significant ($p < 0.05$, two tailed) when zero is not included in the 95% confidence interval (Hayes, 2013; Preacher and Hayes, 2004). The mediation effect size of striatal interconnectivity represented by percent mediation (P_M) was calculated. P_M is interpreted as the percent of the total effect (the effect of nigral iron accumulation on the global attributes of functional network) accounted for by the indirect effect (Preacher and Kelley, 2011).

2.8. Atlas-based validation on functional graph theory analysis

Functional connectivity is defined as the synchronization of rsfMRI signals between predefined brain regions. Functional network construction could be potentially affected by the different brain segmentations (atlases) used in the computations. To minimize the bias resulting from atlas selection, we replicated the functional graph theory analyses in the 2 other atlases (Fig. S2). First, we applied Harvard-Oxford cortical atlas to define 96 cortical parcellations and Harvard-Oxford subcortical atlas to identify 8 main subcortical parcellations bilaterally (e.g., caudate, pallidum, putamen, and thalamus) (https://fsl.fmrib.ox.ac.uk/fsl/fslwiki/Atlases), and then a 104 × 104 functional connectivity matrix per subject was produced. Second, we used a newly constructed cortical atlas (200 parcellations) specifically designed to be in good agreement with architectonic and visuotopic boundaries in rsfMRI data (https://github.com/ThomasYeoLab/CBIG/tree/master/stable_projects/brain_parcellation/Schaefer2018_LocalGlobal) (Schaefer et al., 2018). The same 8 subcortical parcellations were defined by applying the Harvard-Oxford subcortical atlas. In total, a 208 × 208 functional connectivity matrix using this *constructed atlas* was generated for each subject.

3. Results

3.1. Demographic and clinical information

Demographic information and clinical scales are shown in Table 1 for 128 participants. No significant difference was found in age ($p = 0.373$) or gender ($p = 0.164$) between patients with PD and normal controls. Although we excluded 5 patients with potentially cognitive impairment, these recruited patients had a lower MMSE score than normal controls ($p < 0.001$), possibly a result of the lower education in the patient group compared with normal controls ($p < 0.001$). Therefore, in all statistical analyses, we regressed out education as a covariate. For the DTI and rsfMRI database, the distribution of demographic and clinical information between groups was not significantly changed.

Table 1
The distributions of demographic and clinical data and global attributes of functional and structural networks

Variable	Parkinson's disease	Normal controls	*p* value
Demographic and clinical data			
Age, mean ± SD	59.38 ± 8.54	57.93 ± 8.04	0.373
Gender, female/male	40/50	22/16	0.164
MMSE, mean ± SD	26.98 ± 3.77	28.74 ± 1.55	<0.001
Education, mean ± SD	8.36 ± 4.74	11.26 ± 3.90	<0.001
UPDRS III score, mean ± SD	25.91 ± 14.17	0.66 ± 1.12	<0.001
PDQ-39, mean ± SD	23.45 ± 18.50	-	-
Hoehn-Yahr stage, mean ± SD	1.85 ± 0.70	-	-
Disease duration, mean ± SD	3.97 ± 4.09	-	-
Binarized functional networks, mean ± SD			
Global efficiency	0.254 ± 0.007	0.250 ± 0.009	0.013
Characteristic path length	0.891 ± 0.050	0.928 ± 0.066	0.003
Local efficiency	0.347 ± 0.008	0.349 ± 0.010	0.214
Clustering coefficient	0.278 ± 0.010	0.286 ± 0.011	0.001
Weighted functional networks, mean ± SD			
Global efficiency	0.206 ± 0.034	0.227 ± 0.039	<0.001
Characteristic path length	1.052 ± 0.156	0.975 ± 0.154	0.003
Local efficiency	0.304 ± 0.051	0.342 ± 0.058	<0.001
Clustering coefficient	0.116 ± 0.017	0.123 ± 0.018	0.027
Binarized structural networks, mean ± SD			
Global efficiency	0.106 ± 0.002	0.106 ± 0.001	0.412
Characteristic path length	0.380 ± 0.008	0.378 ± 0.005	0.414
Local efficiency	0.137 ± 0.003	0.136 ± 0.003	0.681
Clustering coefficient	0.091 ± 0.003	0.091 ± 0.003	0.944
Weighted structural networks, mean ± SD			
Global efficiency	0.051 ± 0.003	0.051 ± 0.002	0.398
Characteristic path length	0.796 ± 0.051	0.784 ± 0.030	0.375
Local efficiency	0.062 ± 0.003	0.063 ± 0.002	0.546
Clustering coefficient	0.059 ± 0.004	0.059 ± 0.003	0.490

The values of graph metrics shown here are the area under the curve values calculated from the constructed graphs across the selected range of sparsity (for rsfMRI, from 5% to 50% with an interval of 5%; for DTI, from 10% to 30% with an interval of 2%) for each group.
Key: DTI, diffusion tensor imaging; MMSE, Mini–Mental State Examination; PDQ-39, Parkinson's Disease Questionnaire (39 questions); rsfMRI, resting-state functional magnetic resonance imaging; UPDRS, Unified Parkinson's Disease Rating Scale.

3.2. Nigral iron accumulation and their clinical correlations

Among SN subregions (Table 2 and Fig. 3A), the iron distribution was followed by middle part ≈ inferior part > superior part in normal controls. In patients with PD, the distribution of iron was followed by inferior part > middle part > superior part. Similarly, for iron distribution within SNc (Table 2 and Fig. 3B), both patients with PD and normal controls showed a pattern of inferior part > middle part > superior part.

As shown in Fig. 3A, compared with normal controls, significant iron accumulation was specifically observed in the inferior part of the SN ($p = 0.002$) in patients with PD. No significant between-group difference of iron content was found in the superior part ($p = 1.000$) or middle part ($p = 0.228$) of the SN. By detecting clinical relationship of iron accumulation, we observed that iron content in the inferior SN had a significant correlation with PDQ-39 score ($r = 0.319$, $p = 0.002$) (Fig. 3C).

For the predefined SNc (Fig. 3B), significant iron accumulation was observed in the inferior part ($p = 0.009$) in patients with PD, and iron content trended upward in the middle part ($p = 0.032$) compared with normal controls. No obvious increase of iron content was found in the superior part ($p = 0.340$). Clinically, we detected that iron content in the inferior SNc had a significant correlation with PDQ-39 score ($r = 0.484$, $p < 0.001$) (Fig. 3D).

Table 2
The difference of iron distribution among the three subregions of SN and SNc in patients with Parkinson's disease and normal controls

Paired comparisons	Mean of MS differences (ppm)	95% confidence interval	*t* value	*p* value
Normal controls—SN				
Superior SN vs. middle SN	−0.010 ± 0.014	−0.015 ~ −0.006	−4.777	<0.001
Superior SN vs. inferior SN	−0.009 ± 0.021	−0.016 ~ −0.002	−2.652	0.012
Middle SN vs. inferior SN	0.002 ± 0.013	−0.003 ~ +0.006	0.728	0.471
Normal controls—predefined SNc				
Superior SNc vs. middle SNc	−0.012 ± 0.008	−0.014 ~ −0.009	−8.760	<0.001
Superior SNc vs. inferior SNc	−0.037 ± 0.017	−0.042 ~ −0.031	−13.179	<0.001
Middle SNc vs. inferior SNc	−0.025 ± 0.011	−0.029 ~ −0.022	−14.313	<0.001
Patients with Parkinson's disease—SN				
Superior SN vs. middle SN	−0.018 ± 0.013	−0.020 ~ −0.014	−12.472	<0.001
Superior SN vs. inferior SN	−0.028 ± 0.020	−0.032 ~ −0.023	−12.914	<0.001
Middle SN vs. inferior SN	−0.010 ± 0.013	−0.013 ~ −0.007	−7.263	<0.001
Patients with Parkinson's disease—predefined SNc				
Superior SNc vs. middle SNc	−0.018 ± 0.009	−0.020 ~ −0.016	−18.141	<0.001
Superior SNc vs. inferior SNc	−0.049 ± 0.020	−0.054 ~ −0.045	−23.303	<0.001
Middle SNc vs. inferior SNc	−0.032 ± 0.013	−0.034 ~ −0.029	−23.348	<0.001

Key: MS, mean susceptibility; SN, substantia nigra; SNc, SN pars compacta.

Table 3
The mediation effect of striatal interconnectivity in the patients with Parkinson's disease

Independent variable	Mediator	Outcome variable	Indirect effect	Upper and lower bootstrapped 95% confidence interval	Effect size (P_M)
Iron content in the inferior substantia nigra	Striatal interconnectivity	Global efficiency	−0.088	−0.254 ~ −0.004	0.347
		Characteristic path length	0.419	0.029 ~ 1.180	0.440
		Local efficiency	−0.127	−0.359 ~ −0.006	0.286
		Clustering coefficient	−0.036	−0.105 ~ −0.002	0.236

3.3. Impaired subcortical functional connectivity

Among the striatum, pallidum, and thalamus, we compared region-wise functional connectivity between patients with PD and normal controls (Fig. 4). We observed significantly reduced functional connectivity between the bilateral striatums (striatal interconnectivity) in patients with PD patients compared with normal controls ($p < 0.001$). The functional connectivity between the bilateral pallidums had a trend to decrease in patients with PD ($p = 0.035$). However, no clinical correlation was observed.

3.4. Altered global attributes and their clinical correlations

In the binarized functional network (functional skeleton), we observed that, compared with normal controls, patients with PD showed significantly increased global efficiency ($p = 0.013$) but fairly preserved local efficiency ($p = 0.214$) (Table 1 and Figs. 5E and G). The increased global efficiency was significantly correlated with PDQ-39 scores ($r = 0.266$, $p = 0.014$). Moreover, patients with PD had a smaller characteristic path length ($p = 0.003$) and clustering coefficient ($p = 0.001$) than normal controls (Figs. 5F and H), indicating the functional skeleton in patients with PD became globally enhanced but locally impaired.

In the weighted network (topological connectivity), significantly disrupted global efficiency and local efficiency were observed in patients with PD (both $p < 0.001$) (Table 1 and Figs. 6E and G), both of which showed marginal negative correlations with PDQ-39 scores ($r = -0.199$, $p = 0.070$ and $r = -0.216$, $p = 0.049$, respectively). Furthermore, characteristic path length significantly increased ($p = 0.003$) and clustering coefficient tended to reduce ($p = 0.027$) in patients with PD compared with normal controls (Figs. 6F and H). Thus, although the functional skeleton became reorganized to improve the global efficiency, the topological connectivity was disrupted globally and locally in PD.

No significant difference of the global attribute in the binarized and weighted structural networks was observed between patients with PD and normal controls (Table 1). Fig. S3 shows the distributions of global attributes of structural networks.

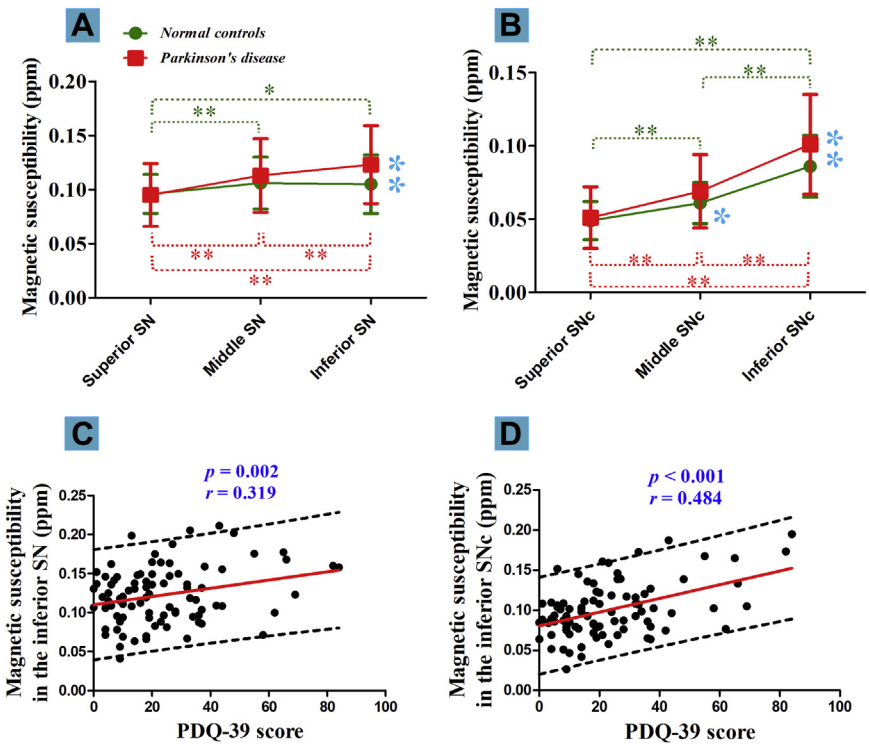

Fig. 3. Iron distribution within SN and the predefined SNc in normal controls and patients with Parkinson's disease. (A) Iron distribution within SN (mean ± standard deviation) and between-group effect of each subregion. (B) Iron distribution within SNc (mean ± standard deviation) and between-group effect of each subregion. (C–D) The significant correlations between nigral iron content and PDQ-39 score. The dark green asterisks show the statistical difference among three subregions in normal controls. The red asterisks show the statistical difference among three subregions in patients. The blue asterisks represent the statistical difference of iron content between normal controls and patients with Parkinson's disease. Single asterisk (*) represents the between-group difference with $p < 0.05$, whereas double asterisks (**) represent the between-group difference with $p < 0.017$ (Bonferroni corrected). Abbreviations: SN, substantia nigra; SNc, SN pars compacta; PDQ-39, Parkinson's Disease Questionnaire (39 questions). (For interpretation of the references to color in this figure legend, the reader is referred to the Web version of this article.)

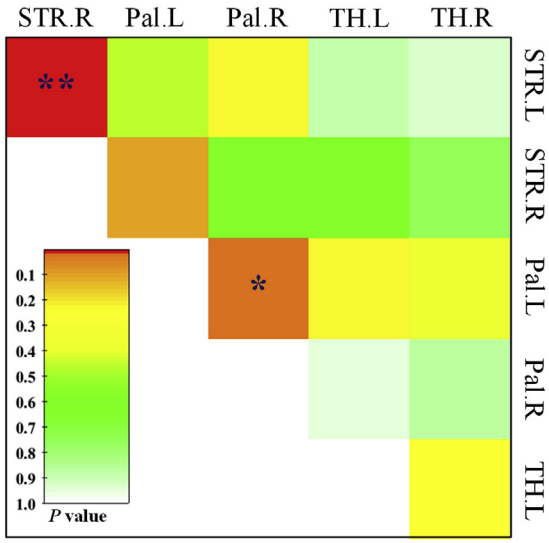

Fig. 4. Intergroup differences of functional connectivity among the striatum, pallidum, and thalamus. This is a *p* value matrix for the intergroup comparisons. Single asterisk (*) represents $p < 0.05$; double asterisk (**) represents $p < 0.003$ (Bonferroni corrected). The color bar shows the numerical *p* value. Abbreviations: L = Left; R = Right; STR = striatum; Pal = pallidum; TH = thalamus. (For interpretation of the references to color in this figure legend, the reader is referred to the Web version of this article.)

3.5. Relationships among nigral iron content, striatal interconnectivity, and global attributes

In the whole population including both patients with PD and normal controls, we observed negative correlation between iron content in the inferior SN and striatal interconnectivity ($r = -0.257$, $p = 0.005$) (Fig. 7, box a). A marginal correlation between them was found in patients with PD ($r = -0.199$, $p = 0.068$). No correlation was observed in normal controls ($r = -0.113$, $p = 0.524$). These results suggested that such correlation might be driven by iron accumulation.

In the binarized network, we detected that iron accumulation in the inferior SN had a significantly positive correlation with functional global efficiency ($r = 0.250$, $p = 0.021$) and negative correlations with functional path length ($r = -0.238$, $p = 0.028$) and clustering coefficient ($r = -0.295$, $p = 0.006$) in patients with PD (Fig. 5I-K). In the weighted network, the increased iron accumulation in the inferior SN was significantly associated with the decreased global efficiency ($r = -0.231$, $p = 0.033$), clustering coefficient ($r = -0.285$, $p = 0.008$), and local efficiency ($r = -0.282$, $p = 0.009$) in patients with PD (Figs. 6I-K).

Based on the opposite trends of global efficiency in the binarized network and weighted network, we supplemented partial correlation analysis between them and found an obviously negative association ($r = -0.420$, $p < 0.001$) in patients with PD; and there was no such correlation in normal controls ($r = -0.172$, $p = 0.330$).

In both normal controls and patients with PD, similar connectivity patterns between striatal interconnectivity and global attributes of weighted functional networks were investigated. In detail, the striatal interconnectivity showed significant correlations with the global efficiency ($r = 0.716$, $p < 0.001$; $r = 0.411$, $p < 0.001$), characteristic path length ($r = -0.656$, $p < 0.001$; $r = -0.423$, $p < 0.001$), local efficiency ($r = 0.728$, $p < 0.001$; $r = 0.412$, $p < 0.001$), and clustering coefficient ($r = 0.594$, $p < 0.001$; $r = 0.347$, $p = 0.001$) in normal controls and patients with PD, respectively (Fig. 7, box c shows the correlation analyses for PD patients).

To observe the nigral iron influence on the functional network in the whole population, we also computed the correlations between iron content in the inferior SN and global attributes of functional networks (Table S1), which were similar to those calculated within the patients with PD.

However, no significant correlation between iron content in the inferior SN and the structural global attribute was found. Thus, our results supported the notion that excessive iron overload in the inferior SN was correlated with the perturbation of functional but not structural networks. No significant correlation was observed between iron accumulation in the inferior SNc and the global attributes of the functional and structural networks.

3.6. Mediation effect of striatal interconnectivity

Significant indirect effects of iron accumulation in the inferior SN on the global attributes of the weighted functional network through striatal interconnectivity in patients with PD were observed. In detail, for the global efficiency, the indirect effect was −0.088 (95% confidence interval was −0.254 to −0.004) and the P_M was 0.347; for the local efficiency, the indirect effect was −0.127 (95% confidence interval was −0.359 to −0.006) and the P_M was 0.286; for characteristic path length, the indirect effect was 0.419 (95% confidence interval was 0.029–1.180) and the P_M was 0.440; and for the clustering coefficient, the indirect effect was −0.036 (95% confidence interval was −0.105 to −0.002) and the P_M was 0.236. There was no significant mediation effect of striatal interconnectivity on the global attributes of the binarized functional network in patients with PD. No significant mediation effect of striatal interconnectivity on the binarized and weighted functional networks in normal controls was observed. In summary, through mediation analysis, we found that striatal dysfunction might be a potential mediator to modulate the influence of iron-related nigral degeneration on the global configuration of the weighted functional network in patients with PD (Table 3).

3.7. Robustness of findings on functional network calculation across different atlases

The aforementioned findings were generally stable across different brain segmentations (Fig. S2).

3.7.1. Binarized functional network alterations

Compared with normal controls, we observed that the global efficiency was similarly increased with decreased characteristic path length in patients with PD (Table S2). Significantly decreased clustering coefficient was seen in the constructed atlas. The relationships of iron content in the inferior SN with these altered global attributes were replicated (Table S3).

3.7.2. Weighted functional network alterations

Globally and locally disrupted functional topologies were identically investigated in patients with PD (Table S2), and their correlations with nigral iron accumulation were observed (Table S3).

3.7.3. Striatal dysfunction identified by using the Harvard-Oxford subcortical atlas

Functional connectivity between the bilateral striatums was significantly reduced (Bonferroni corrected), whereas functional connectivity between the bilateral pallidums tended to decrease ($0.003 < p < 0.05$) in patients with PD compared with normal controls (Table S4). In the whole population, correlation of striatal interconnectivity with iron content in the inferior SN was robustly detected ($r = -0.254$, $p = 0.005$) (Fig. S4).

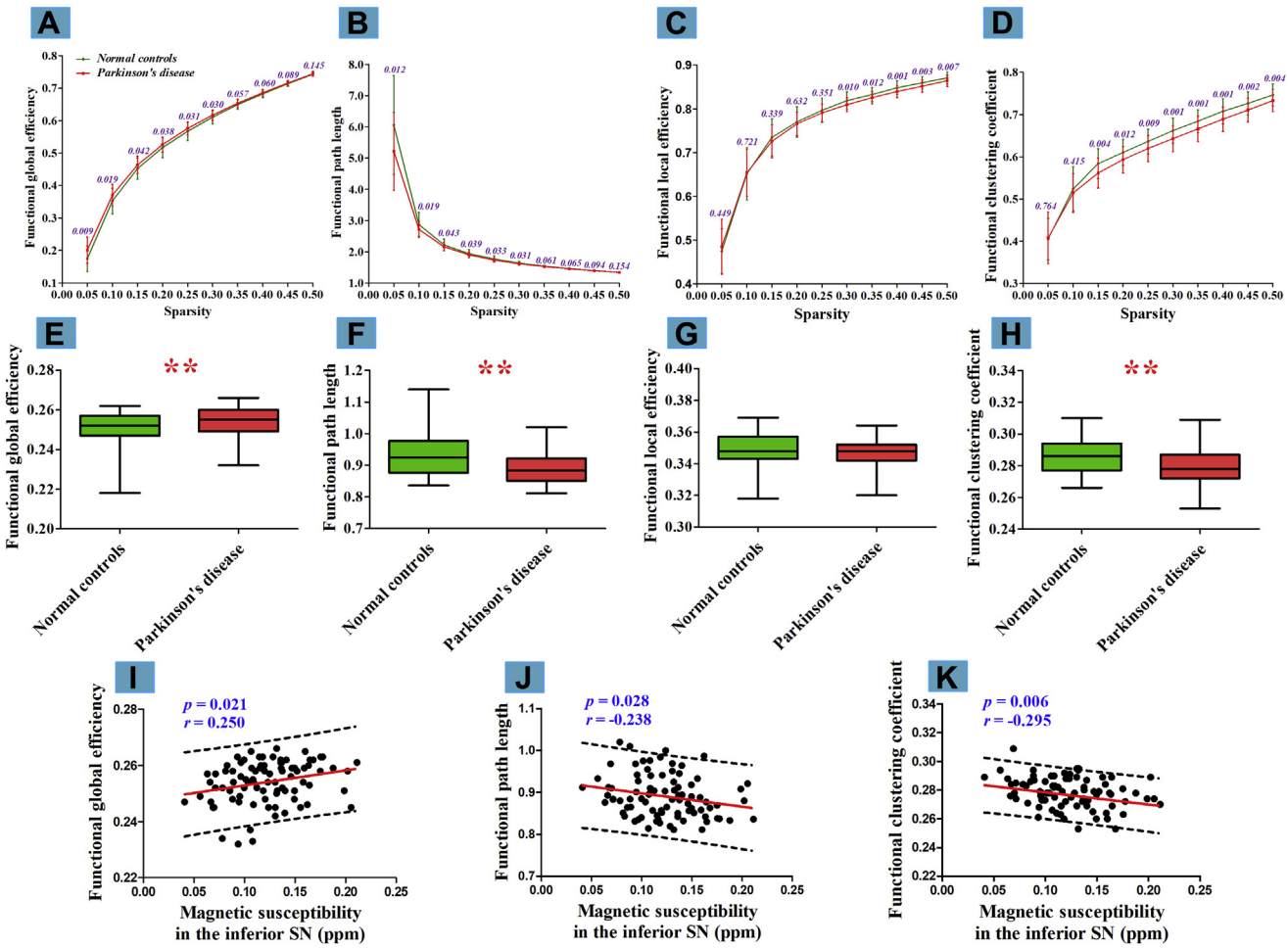

Fig. 5. Intergroup differences in global attributes of binarized functional networks and their correlations with nigral iron content. (A–D) Global attributes of binarized functional networks (mean ± standard deviation) in normal controls and patients with Parkinson's disease over the selected range of sparsity. The *p* values in these subfigures are representing the significances of intergroup comparisons of the global attributes in each selected sparsity. (E–H) Altered AUC values of global attributes of binarized functional networks in patients with Parkinson's disease compared with normal controls. Each boxplot is displaying the distribution of data based on a five-number summary ("minimum", first quartile, median, third quartile, and "maximum"). Single asterisk (*) represents $p < 0.05$; double asterisks (**) represent $p < 0.013$ (Bonferroni corrected). (I–K) The linear correlations between nigral iron content and altered global attributes of binarized functional networks. Abbreviations: AUC, area under the curve; SN, substantia nigra.

3.7.4. Relationships between striatal interconnectivity and weighted global attributes

In agreement with results using the AAL atlas, close correlations of striatal interconnectivity with functional topology computed by using atlases with 208 nodes and 104 nodes were observed (Table S5).

3.7.5. Clinical correlations of altered global attributes

We found stable correlations between global efficiency of the binarized functional network and PDQ-39 score (Table S6).

3.7.6. Mediation effect of striatal interconnectivity in PD

Similarly, we observed significant indirect effects of nigral iron accumulation in the inferior SN on the 4 global attributes of weighted functional networks defined by both atlases through striatal interconnectivity segmented by the Harvard-Oxford subcortical atlas (Table S7).

4. Discussion

In this study, we identified a potential pathway linking iron-related nigral degeneration to global disruption of weighted functional network mediated by striatal dysfunction in PD. In detail, we obtained the following findings: (1) the middle to inferior parts of SN and predefined SNc were susceptible to iron overload in both normal controls and patients with PD, and significant iron accumulation showing positive correlations with PDQ-39 was specifically observed in the inferior parts in PD; (2) in the binarized functional network, enhanced global efficiency and reduced clustering coefficient were identified while in the weighted functional network both global and local efficiencies were reduced in patients with PD, most of these altered global attributes had significant correlations with nigral iron accumulation; (3) striatal interconnectivity disrupted in patients with PD was demonstrated to be a mediator in the potential pathway from iron accumulation in the inferior SN to global perturbation of weighted functional network in PD; (4) we did not observe any alteration in both binarized and weighted structural networks in patients with PD.

4.1. Specific iron accumulation in the inferior substantia nigra in PD

The cause of neuronal death in the iron-rich SN is still unclear. Iron concentration in the human SN dramatically increases in the first 2 decades and is maintained for the rest of the life span

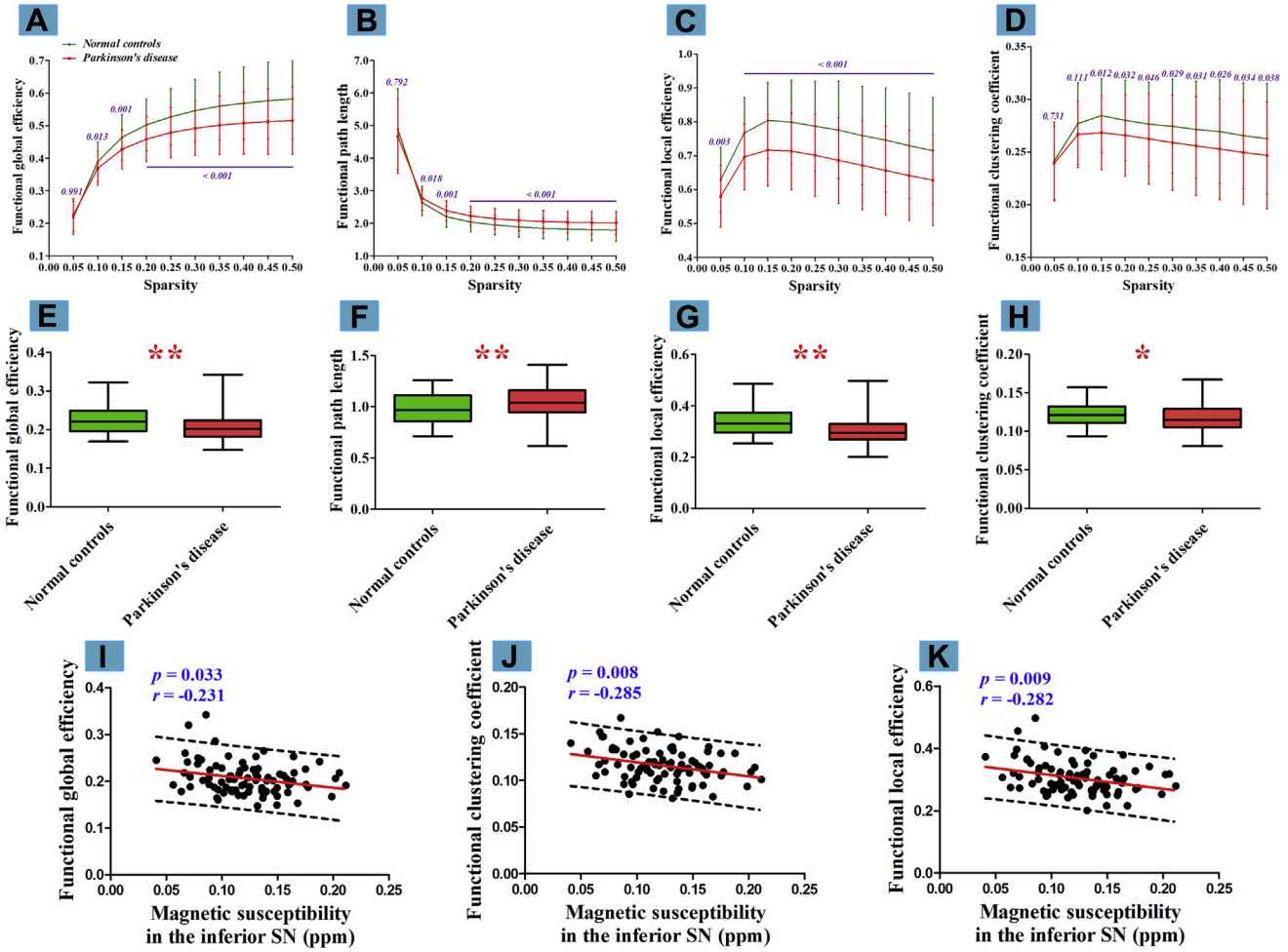

Fig. 6. Intergroup differences in global attributes of weighted functional networks and their correlations with nigral iron content. (A–D) Global attributes of weighted functional networks (mean ± standard deviation) in normal controls and patients with Parkinson's disease over the selected range of sparsity. The *p* values in these subfigures are representing the significances of intergroup comparisons of the global attributes in each selected sparsity. (E–H) Altered AUC values global attributes of weighted functional networks in patients with Parkinson's disease compared with normal controls. Each boxplot is displaying the distribution of data based on a five-number summary ("minimum", first quartile, median, third quartile, and "maximum"). Single asterisk (*) represents $p < 0.05$; double asterisks (**) represent $p < 0.013$ (Bonferroni corrected). (I–K) The linear correlations between nigral iron content and altered global attributes of weighted functional networks. Abbreviations: AUC, area under the curve; SN, substantia nigra.

(Hallgren and Sourander, 1958; Xu et al., 2008; Zecca et al., 2001). Aging is the major risk factor for PD (Pringsheim et al., 2014), and the misregulation of iron homeostasis in the later decades of life and its induced oxidative stress and free radical formation may trigger a cascade of deleterious events leading to neuronal death and the ensuing biochemical disturbances of clinical relevance (Jellinger, 1999; Ward et al., 2014). Moreover, iron depositing within the SN is far from homogeneous. Both postmortem staining and in vivo QSM measurement suggested that iron content in the caudal slices is higher than that in the cranial slices (Lotfipour et al., 2012; Massey et al., 2017). In the present study, we also observed that the iron distribution within the SN followed the pattern of "middle part ≈ inferior part > superior part" in normal controls, whereas it followed the pattern of "inferior part > middle part > superior part" in patients with PD. Therefore, we speculate that the caudal SN, especially the inferior SN, is more liable to iron overload, which indicates that neurons in this subregion are susceptible to high oxidative stress and α-synuclein aggregation (Jellinger, 1999; Ostrerova-Golts et al., 2000; Wan et al., 2017; Ward et al., 2014).

Specifically, we observed significant iron accumulation in the inferior SN in PD, which had positive correlation with disease severity measured by PDQ-39. It has been well known that the severest and earliest degeneration of dopaminergic neurons occurs in the inferior (caudal) SN (Damier et al., 1999). Thus, a possible explanation for our findings is that the high iron-induced oxidative stress and α-synuclein aggregation may have a strong correlation with the neuronal loss in this subregion. As known to us, a number of studies have reported nigral iron accumulation in different stages of PD (Acosta-Cabronero et al., 2017; Guan et al., 2017a; He et al., 2015; Jin et al., 2011; Langkammer et al., 2016; Peran et al., 2010). *Du* et al. manually bisected the SN and found significant iron accumulation in the both caudal and rostral parts by using R2* mapping with the caudal SN having more iron content than rostral counterpart (Du et al., 2012). In an explorative 7.0-Tesla QSM study, *Lotfipour* et al. detected an increased gradient of iron distribution along the rostral to caudal axis, but the significant between-group difference did not survive after regressing out the covariate (Lotfipour et al., 2012). In comparison to the potential bias induced by the R2* mapping with noisy background signal and the manual measurement of iron content in the SN subregions (Du et al., 2012), the normalization of the individual QSM images to an age-specific QSM template performed in our study could help minimize the bias. In addition, the small sample sizes included in these studies (Du et al., 2012; Lotfipour et al., 2012) might also lead to the

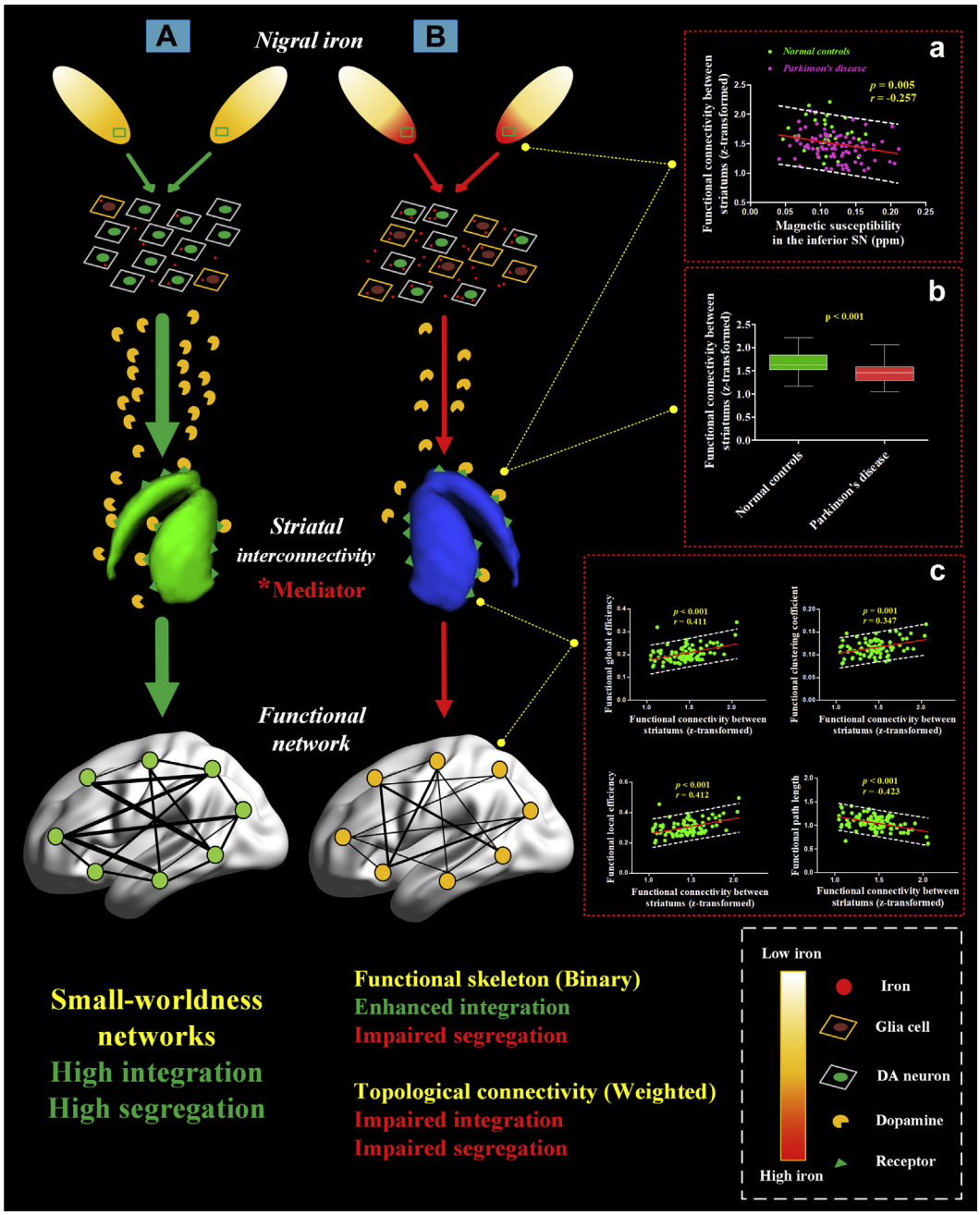

Fig. 7. A hypothesized pathway from iron-related nigral degeneration to functional topology mediated by striatal dysfunction for Parkinson's disease. Pathway (A) exhibits the normal nigral iron distribution and the typical dopaminergic nigrostriatal pathway, which we postulate to play a role in preserving small-worldness of the functional network. Based on the demonstrated associations among nigral iron content, striatal interconnectivity and functional topological connectivity, and the mediation effect of striatal interconnectivity in the present study, pathway (B) potentially describes a hypothesized pathogenesis from the nigral iron accumulation (a proposed disease source) to the global perturbation of the functional network possibly mediated by dysfunction of striatal interconnectivity. According to the historical literature, the nigral iron accumulation may break the local balance of oxidative stress system and contribute to α-synuclein aggregation in SN (Wan et al., 2017; Ward et al., 2014) thus leading to the degeneration of the DA neurons companying with the activated neuroglia cells (e.g., microglia infiltration) (Xu et al., 2017). (Box a) shows the negative correlation of nigral iron content with the functional connectivity between bilateral striatums (striatal interconnectivity) in the whole population. (Box b) contains boxplots revealing the significance of the impairment of striatal interconnectivity in Parkinson's disease. (Box c) shows four functional graph metrics plotted against striatal interconnectivity to reveal the crucial role that the striatal interconnectivity plays in connecting with the weighted functional network in Parkinson's disease. "*" represents that the striatal interconnectivity possibly is a mediator in the pathway from iron-related nigral degeneration to global perturbation of weighted functional network. The boxplot in Box b is displaying the distribution of data based on a five-number summary ("minimum", first quartile, median, third quartile, and "maximum"). Abbreviation: DA neuron, dopaminergic neuron.

inconsistencies. Furthermore, we observed that the only clinical scale significantly correlated with iron accumulation in the inferior SN was PDQ-39, which was a validated comprehensive means to evaluate the influence of motor and nonmotor symptoms on the life quality including mobility, activities of daily living, emotional well-being, stigma, social support, cognitions, communication, and bodily discomfort specifically for patients with PD (Den Oudsten et al., 2007; Peto et al., 1995). It is commonly recognized that both motor and nonmotor symptoms are extensively involved (Lees et al., 2009) due to the global depletion of dopamine and the

widespread aggregation of α-synuclein (Braak et al., 2003; Kish et al., 1988). Therefore, PDQ-39 could be indicative of the global dysfunction and progression of PD. It is worth noting that, although it was still less consistent about the influence of nigral iron accumulation on clinical relevance, e.g., UPDRS part III score (specific motor symptoms) (Du et al., 2012; Guan et al., 2017a; He et al., 2015; Jin et al., 2011; Martin et al., 2008) and UPDRS part II score (global function impairment) (Du et al., 2016; Langkammer et al., 2016; Xuan et al., 2017), all of these scales including PDQ-39 have the ability to reflect the disease progression relating to the pathological burden in PD. In summary, by using an unbiased QSM template to measure nigral iron content, this study demonstrated that the inferior SN was specifically involved with significant iron accumulation in PD, which was strongly correlated with disease severity.

4.2. The influence of nigral iron accumulation on the functional topology is mediated by striatal interconnectivity

Studies have suggested that the basal ganglia, especially the striatum (Kish et al., 1988), are typically the main structure perturbed by the depletion of dopamine. We detected impaired functional connectivity between the bilateral striatums in patients with PD compared with normal controls. Because no significant correlation was observed with clinical symptoms, a floor effect of disruption in this connectivity was suspected, which indicated a nonlinear progression between neuronal death and striatal dysfunction. Considering iron-related nigral degeneration had a close relation to disease severity discussed previously, the absence of significant correlation ($p = 0.068$) between nigral iron accumulation and striatal interconnectivity in patients with PD might be expectable. Consistent with this notion, significantly negative correlation between the nigral iron content and the striatal interconnectivity was observed in the whole population. Although the causal relationship between nigral iron accumulation and loss of dopaminergic neurons is not fully known, excessive iron overload has been postulated to be a causative factor in PD through iron-induced oxidative stress, neurotoxicity of α-synuclein aggregation, and neuronal vulnerability (Jellinger, 1999; Ostrerova-Golts et al., 2000; Wan et al., 2017; Ward et al., 2014). Therefore, assuming the negative influences of nigral iron accumulation on the dopaminergic neurons are temporal continuum (from normal to parkinsonian), our findings indicate that iron-related nigral degeneration in PD potentially triggers the dysfunction of the nigrostriatal pathway, which is highly depending on dopaminergic modulation. At the network level, we observed that the striatal interconnectivity was strongly correlated with the global integration and local segregation of the weighted network in both patients with PD and normal controls. In agreement with our findings, previous work showed that striatal dysfunction contributed to connectivity impairments in multiple large-scale cerebral networks in PD (Bell et al., 2015; Shine et al., 2013a,b), which could be partially reversed by dopamine therapy (Bell et al., 2015). We speculate that this connectivity pattern underlines a functional underpinning such that striatal interconnectivity plays a potentially important role in connecting with the configuration of weighted functional network.

We then investigated the global alterations of functional networks in PD. In the binarized functional network, significantly increased global efficiency and decreased clustering coefficient were detected in patients with PD compared with normal controls, which indicated enhanced integration and impaired segregation of the functional skeleton in patients with PD (Liao et al., 2017; Watts and Strogatz, 1998). This finding was consistent with several studies that have reported observable alterations of the binarized functional network in PD. *Fang* et al. found that the functional network in patients with PD expressed lower path length and clustering coefficient (increased global integration and decreased local segregation) compared with normal controls (Fang et al., 2017), and *Luo* et al. observed decreased clustering coefficient (local efficiency) in patients with PD (Luo et al., 2015). Although no between-group difference of the global attribute was observed, dopamine therapy could impart a normalized effect on global and local efficiency through significantly reducing this couple of global attributes (Berman et al., 2016). Different from the binarized network, the weighted functional network takes into account connectivity strength (Berman et al., 2016; Ginestet et al., 2011; Liao et al., 2017). Surprisingly, although the local segregation of the weighted functional network decreased in agreement with the binarized network, the weighted global integration was found to be disrupted. However, this finding was consistent with the *Skidmore* et al. study, which studied the first weighted network in patients with PD and demonstrated significantly decreased overall network efficiency (Skidmore et al., 2011). In combination with the negative correlation between the binarized and weighted global efficiencies, these results complement an emerging view of a trade-off modulation that the functional skeleton continuously reorganizes to increase effective communication across all pairs of nodes when the topological connectivity is disrupted globally and locally in PD.

Subsequently, we explored whether the relationships between iron-related nigral degeneration and global networks were present in PD. Plausibly, we observed significant associations between the nigral iron accumulation and the disorganized global functional networks in PD. Furthermore, we found that the striatal interconnectivity had significant mediation effect on such association between iron-related degeneration and global perturbation of the weighted functional network. Therefore, although the exact causality of the demonstrated associations among nigral iron, striatal interconnectivity, and global network needs further validation, we move forward to hypothesize a potential pathway that iron-related nigral degeneration (a proposed disease source) may negatively influence the functional topology mediated by striatal dysfunction, which may play a crucial role in PD pathogenesis (overview in Fig. 7).

4.3. No significant alteration of global configuration of the structural network in PD

However, we did not observe any alteration of global attribute in the both binarized and weighted structural networks, nor any correlation between global structural attributes and nigral iron accumulation. The global attributes of structural networks were not commonly damaged through DTI and T1-weighted imaging data (Galantucci et al., 2017; Pereira et al., 2015; Wen et al., 2017; Xu et al., 2018) in PD without evidence of cognitive impairment, which subsequently were disrupted in the patients with cognitive deficits (Galantucci et al., 2017; Pereira et al., 2015). Paradoxically, some studies also reported increased path length (decreased global efficiency) (Abbasi et al., 2018; Li et al., 2017; Nigro et al., 2016) in PD. Because motor and nonmotor symptoms are both commonly observed in PD, the alterations of structural networks are symptom dependent, which may explain the inconsistencies. In our opinion, this multimodality investigation demonstrated that the altered functional network in PD may precede or may be more sensitive than an underlying alteration of the structural network.

4.4. Reproducible iron accumulation in the predefined SNc in PD

By automatically extracting iron content based on the normalized QSM maps, we performed a reproducible analysis similar as the previous studies using manual measurement of iron content in

the predefined SNc (Du et al., 2016; Guan et al., 2017b,d; Martin et al., 2008; Wang et al., 2013; Xuan et al., 2017). Similar to the SN, the iron distribution gradient of "inferior part > middle part > superior part" was detected within SNc in both patients with PD and normal controls. We observed significant iron accumulation in the inferior subregion, and its iron content had a significant correlation with the PDQ-39 score (global dysfunction). These findings agreed with previous studies that reported iron accumulation in this predefined SNc in PD (Du et al., 2016; Guan et al., 2017b; Martin et al., 2008; Wang et al., 2013) and iron accumulation in this SNc characterized PD independent of the motor subtypes (i.e., akinesia/rigidity-dominant and tremor-dominant) (Guan et al., 2017d) and the age of onset (i.e., early-onset and middle-late-onset) (Xuan et al., 2017). Nevertheless, because the identification of the SN, SNc, and SN pars reticulata (SNr) in MR images remains largely controversial (Acosta-Cabronero et al., 2017; Barbosa et al., 2015; Du et al., 2012; Du et al., 2016; Guan et al., 2017b,d; He et al., 2015; Jin et al., 2011; Langkammer et al., 2016; Lotfipour et al., 2012), in this study, we used SN and predefined SNc as separate terms to maximally unify the definitions published historically. Future investigations using histology and ultrahigh field MRI may be helpful to achieve more accurate segmentations and validate their biological basis.

4.5. Limitations

There were several limitations in the present study. First, the in vivo iron quantification of MRI technology has limitations in differentiating the ferrous and ferric iron, the intracellular and extracellular iron, and the involved cell types (e.g., microglia, oligodendroglia, and neurons) (Liu et al., 2015; Wang and Liu, 2015; Xu et al., 2017). Therefore, researchers should be cautious when translating our results beyond the voxel level. Second, since this was the first study to explain a potential pathway associating iron-related nigral degeneration with striatal dysfunction and global network disruption in PD by employing multimodality MRI, studies using other bioelectrical technologies, such as the echoencephalogram and electroencephalograph, may be worthwhile for further validation of our findings. Third, from histological documents, it is well established that pathogeneses associated with global perturbation in PD are widespread and complex (Braak et al., 2003; Jucker and Walker, 2013). Presently, we focused on in vivo evidence for explaining the dopaminergic pathway associating with iron-related nigral degeneration. Recent work demonstrated the role of the noradrenergic system in the network integration (Shine et al., 2016, 2018) and its disruption in PD (Peterson and Li, 2018). Therefore, future studies are necessary to interrogate the mechanism of the noradrenergic system to reach a thorough understanding of PD pathogenesis.

5. Conclusions

Our results suggest that nigral iron accumulation, specifically in the inferior part, is one of the core pathological alterations in PD. By taking advantages of multimodality MRI information, our in vivo findings demonstrate that iron-related nigral degeneration possibly influences the functional topology mediated by striatal dysfunction, which extends the scientific understanding of PD pathogenesis.

Disclosure

The authors have no actual or potential conflicts of interest.

Acknowledgements

The authors thank all the normal volunteers and PD patients recruited in this project. The authors appreciate Prof. Jinhui Wang (Hangzhou Normal University, China) for his suggestions on graph theory analysis and Steven Cao (University of California, Berkeley, USA) for linguistic editing.

Funding: This work is supported by the 13th Five-year Plan for National Key Research and Development Program of China (Grant No. 2016YFC1306600), the National Natural Science Foundation of China (Grant No. 81571654, 81371519, 81701647 and 81771820), the 12th Five-year Plan for National Science and Technology Supporting Program of China (Grant No. 2012BAI10B04), the Fundamental Research Funds for the Central Universities of China (Grant No. 2017XZZX001-01), the Natural Science Foundation of Zhejiang Province (Grant No. LY17H090020), and the Projects of Medical and Health Technology Development Program in Zhejiang Province (Grant No. 2015KYB174). CL is supported in part by US National Institutes of Health (Grant No. R01MH096979).

Appendix A. Supplementary data

Supplementary data to this article can be found online at https://doi.org/10.1016/j.neurobiolaging.2018.11.013.

References

Abbasi, N., Mohajer, B., Abbasi, S., Hasanabadi, P., Abdolalizadeh, A., Rajimehr, R., 2018. Relationship between cerebrospinal fluid biomarkers and structural brain network properties in Parkinson's disease. Mov. Disord. 33, 431–439.
Acosta-Cabronero, J., Cardenas-Blanco, A., Betts, M.J., Butryn, M., Valdes-Herrera, J.P., Galazky, I., Nestor, P.J., 2017. The whole-brain pattern of magnetic susceptibility perturbations in Parkinson's disease. Brain 140, 118–131.
Barbosa, J.H., Santos, A.C., Tumas, V., Liu, M., Zheng, W., Haacke, E.M., Salmon, C.E., 2015. Quantifying brain iron deposition in patients with Parkinson's disease using quantitative susceptibility mapping, R2 and R2. Magn. Reson. Imaging 33, 559–565.
Bell, P.T., Gilat, M., O'Callaghan, C., Copland, D.A., Frank, M.J., Lewis, S.J., Shine, J.M., 2015. Dopaminergic basis for impairments in functional connectivity across subdivisions of the striatum in Parkinson's disease. Hum. Brain Mapp. 36, 1278–1291.
Berman, B.D., Smucny, J., Wylie, K.P., Shelton, E., Kronberg, E., Leehey, M., Tregellas, J.R., et al., 2016. Levodopa modulates small-world architecture of functional brain networks in Parkinson's disease. Mov. Disord. 31, 1676–1684.
Bilgic, B., Pfefferbaum, A., Rohlfing, T., Sullivan, E.V., Adalsteinsson, E., 2012. MRI estimates of brain iron concentration in normal aging using quantitative susceptibility mapping. Neuroimage 59, 2625–2635.
Braak, H., Del, T.K., Rub, U., de Vos, R.A., Jansen, S.E., Braak, E., 2003. Staging of brain pathology related to sporadic Parkinson's disease. Neurobiol. Aging 24, 197–211.
Bullmore, E.T., Bassett, D.S., 2011. Brain graphs: graphical models of the human brain connectome. Annu. Rev. Clin. Psychol. 7, 113–140.
Cui, Z., Zhong, S., Xu, P., He, Y., Gong, G., 2013. PANDA: a pipeline toolbox for analyzing brain diffusion images. Front Hum. Neurosci. 7, 42.
Damier, P., Hirsch, E.C., Agid, Y., Graybiel, A.M., 1999. The substantia nigra of the human brain. II. Patterns of loss of dopamine-containing neurons in Parkinson's disease. Brain 122 (Pt 8), 1437–1448.
Den Oudsten, B.L., Van Heck, G.L., De Vries, J., 2007. The suitability of patient-based measures in the field of Parkinson's disease: a systematic review. Mov Disord. 22, 1390–1401.
Dexter, D.T., Carayon, A., Javoy-Agid, F., Agid, Y., Wells, F.R., Daniel, S.E., Lees, A.J., Jenner, P., Marsden, C.D., 1991. Alterations in the levels of iron, ferritin and other trace metals in Parkinson's disease and other neurodegenerative diseases affecting the basal ganglia. Brain 114 (Pt 4), 1953–1975.
Du, G., Lewis, M.M., Sen, S., Wang, J., Shaffer, M.L., Styner, M., Yang, Q.X., Huang, X., 2012. Imaging nigral pathology and clinical progression in Parkinson's disease. Mov Disord. 27, 1636–1643.
Du, G., Liu, T., Lewis, M.M., Kong, L., Wang, Y., Connor, J., Mailman, R.B., Huang, X., 2016. Quantitative susceptibility mapping of the midbrain in Parkinson's disease. Mov Disord. 31, 317–324.
Fang, J., Chen, H., Cao, Z., Jiang, Y., Ma, L., Ma, H., Feng, T., 2017. Impaired brain network architecture in newly diagnosed Parkinson's disease based on graph theoretical analysis. Neurosci. Lett. 657, 151–158.
Galantucci, S., Agosta, F., Stefanova, E., Basaia, S., van den Heuvel, M.P., Stojkovic, T., Canu, E., Stankovic, I., Spica, V., Copetti, M., Gagliardi, D., Kostic, V.S., Filippi, M., 2017. Structural brain connectome and cognitive impairment in Parkinson disease. Radiology 283, 515–525.

Ginestet, C.E., Nichols, T.E., Bullmore, E.T., Simmons, A., 2011. Brain network analysis: separating cost from topology using cost-integration. PLoS One 6, e21570.
Gong, G., He, Y., Concha, L., Lebel, C., Gross, D.W., Evans, A.C., Beaulieu, C., 2009. Mapping anatomical connectivity patterns of human cerebral cortex using in vivo diffusion tensor imaging tractography. Cereb. Cortex 19, 524–536.
Guan, X., Zeng, Q., Guo, T., Wang, J., Xuan, M., Gu, Q., Wang, T., Huang, P., Xu, X., Zhang, M., 2017a. Disrupted functional connectivity of basal ganglia across tremor-dominant and Akinetic/Rigid-dominant Parkinson's disease. Front Aging Neurosci. 9, 360.
Guan, X., Xuan, M., Gu, Q., Huang, P., Liu, C., Wang, N., Xu, X., Luo, W., Zhang, M., 2017b. Regionally progressive accumulation of iron in Parkinson's disease as measured by quantitative susceptibility mapping. NMR Biomed. 30, e3489.
Guan, X., Xu, X., Zhang, M., 2017c. Region-specific iron measured by MRI as a biomarker for Parkinson's disease. Neurosci. Bull 33, 561–567.
Guan, X., Xuan, M., Gu, Q., Xu, X., Huang, P., Wang, N., Shen, Z., Xu, J., Luo, W., Zhang, M., 2017d. Influence of regional iron on the motor impairments of Parkinson's disease: a quantitative susceptibility mapping study. J. Magn. Reson. Imaging 45, 1335–1342.
Hallgren, B., Sourander, P., 1958. The effect of age on the non-haemin iron in the human brain. J. Neurochem. 3, 41–51.
Hayes, A.F., 2013. Introduction to Mediation, Moderation, and Conditional Process Analysis: A Regression-based Approach. Guilford Press, New York.
He, N., Ling, H., Ding, B., Huang, J., Zhang, Y., Zhang, Z., Liu, C., Chen, K., Yan, F., 2015. Region-specific disturbed iron distribution in early idiopathic Parkinson's disease measured by quantitative susceptibility mapping. Hum. Brain Mapp. 36, 4407–4420.
Hughes, A.J., Daniel, S.E., Kilford, L., Lees, A.J., 1992. Accuracy of clinical diagnosis of idiopathic Parkinson's disease: a clinico-pathological study of 100 cases. J. Neurol. Neurosurg. Psychiatry 55, 181–184.
Jellinger, K., Paulus, W., Grundke-Iqbal, I., Riederer, P., Youdim, M.B., 1990. Brain iron and ferritin in Parkinson's and Alzheimer's diseases. J. Neural Transm. Park Dis. Dement. Sect. 2, 327–340.
Jellinger, K.A., 1999. The role of iron in neurodegeneration: prospects for pharmacotherapy of Parkinson's disease. Drugs Aging 14, 115–140.
Jin, L., Wang, J., Zhao, L., Jin, H., Fei, G., Zhang, Y., Zeng, M., Zhong, C., 2011. Decreased serum ceruloplasmin levels characteristically aggravate nigral iron deposition in Parkinson's disease. Brain 134, 50–58.
Jucker, M., Walker, L.C., 2013. Self-propagation of pathogenic protein aggregates in neurodegenerative diseases. Nature 501, 45–51.
Katzman, R., Zhang, M.Y., Ouang-Ya-Qu, Wang, Z.Y., Liu, W.T., Yu, E., Wong, S.C., Salmon, D.P., Grant, I., 1988. A Chinese version of the Mini-Mental State Examination; impact of illiteracy in a Shanghai dementia survey. J. Clin. Epidemiol. 41, 971–978.
Kish, S.J., Shannak, K., Hornykiewicz, O., 1988. Uneven pattern of dopamine loss in the striatum of patients with idiopathic Parkinson's disease. Pathophysiologic and clinical implications. N. Engl. J. Med. 318, 876–880.
Langkammer, C., Pirpamer, L., Seiler, S., Deistung, A., Schweser, F., Franthal, S., Homayoon, N., Katschnig-Winter, P., Koegl-Wallner, M., Pendl, T., Stoegerer, E.M., Wenzel, K., Fazekas, F., Ropele, S., Reichenbach, J.R., Schmidt, R., Schwingenschuh, P., 2016. Quantitative susceptibility mapping in Parkinson's disease. PLoS One 11, e0162460.
Langkammer, C., Schweser, F., Krebs, N., Deistung, A., Goessler, W., Scheurer, E., Sommer, K., Reishofer, G., Yen, K., Fazekas, F., Ropele, S., Reichenbach, J.R., 2012. Quantitative susceptibility mapping (QSM) as a means to measure brain iron? A post mortem validation study. Neuroimage 62, 1593–1599.
Lees, A.J., Hardy, J., Revesz, T., 2009. Parkinson's disease. Lancet 373, 2055–2066.
Li, C., Huang, B., Zhang, R., Ma, Q., Yang, W., Wang, L., Wang, L., Xu, Q., Feng, J., Liu, L., Zhang, Y., Huang, R., 2017. Impaired topological architecture of brain structural networks in idiopathic Parkinson's disease: a DTI study. Brain Imaging Behav. 11, 113–128.
Li, W., Avram, A.V., Wu, B., Xiao, X., Liu, C., 2014. Integrated Laplacian-based phase unwrapping and background phase removal for quantitative susceptibility mapping. NMR Biomed. 27, 219–227.
Li, W., Wang, N., Yu, F., Han, H., Cao, W., Romero, R., Tantiwongkosi, B., Duong, T.Q., Liu, C., 2015. A method for estimating and removing streaking artifacts in quantitative susceptibility mapping. Neuroimage 108, 111–122.
Liao, X., Vasilakos, A.V., He, Y., 2017. Small-world human brain networks: Perspectives and challenges. Neurosci. Biobehav Rev. 77, 286–300.
Liu, C., Li, W., Tong, K.A., Yeom, K.W., Kuzminski, S., 2015. Susceptibility-weighted imaging and quantitative susceptibility mapping in the brain. J. Magn. Reson. Imaging 42, 23–41.
Lotfipour, A.K., Wharton, S., Schwarz, S.T., Gontu, V., Schafer, A., Peters, A.M., Bowtell, R.W., Auer, D.P., Gowland, P.A., Bajaj, N.P., 2012. High resolution magnetic susceptibility mapping of the substantia nigra in Parkinson's disease. J. Magn. Reson. Imaging 35, 48–55.
Lu, F.M., Dai, J., Couto, T.A., Liu, C.H., Chen, H., Lu, S.L., Tang, L.R., Tie, C.L., Chen, H.F., He, M.X., Xiang, Y.T., Yuan, Z., 2017. Diffusion tensor imaging tractography reveals disrupted white matter structural connectivity network in healthy adults with insomnia symptoms. Front Hum. Neurosci. 11, 583.
Luo, C.Y., Guo, X.Y., Song, W., Chen, Q., Cao, B., Yang, J., Gong, Q.Y., Shang, H.F., 2015. Functional connectome assessed using graph theory in drug-naive Parkinson's disease. J. Neurol. 262, 1557–1567.
Martin, W.R., Wieler, M., Gee, M., 2008. Midbrain iron content in early Parkinson disease: a potential biomarker of disease status. Neurology 70, 1411–1417.
Massey, L.A., Miranda, M.A., Al-Helli, O., Parkes, H.G., Thornton, J.S., So, P.W., White, M.J., Mancini, L., Strand, C., Holton, J., Lees, A.J., Revesz, T., Yousry, T.A., 2017. 9.4 T MR microscopy of the substantia nigra with pathological validation in controls and disease. Neuroimage Clin. 13, 154–163.
Mori, S., Crain, B.J., Chacko, V.P., van Zijl, P.C., 1999. Three-dimensional tracking of axonal projections in the brain by magnetic resonance imaging. Ann. Neurol. 45, 265–269.
Muldoon, S.F., Bridgeford, E.W., Bassett, D.S., 2016. Small-World Propensity and weighted brain networks. Sci. Rep. 6, 22057.
Nigro, S., Riccelli, R., Passamonti, L., Arabia, G., Morelli, M., Nistico, R., Novellino, F., Salsone, M., Barbagallo, G., Quattrone, A., 2016. Characterizing structural neural networks in de novo Parkinson disease patients using diffusion tensor imaging. Hum. Brain Mapp. 37, 4500–4510.
Obeso, J.A., Rodriguez-Oroz, M.C., Rodriguez, M., Lanciego, J.L., Artieda, J., Gonzalo, N., Olanow, C.W., 2000. Pathophysiology of the basal ganglia in Parkinson's disease. Trends Neurosci. 23, S8–S19.
Ostrerova-Golts, N., Petrucelli, L., Hardy, J., Lee, J.M., Farer, M., Wolozin, B., 2000. The A53T alpha-synuclein mutation increases iron-dependent aggregation and toxicity. J. Neurosci. 20, 6048–6054.
Peran, P., Cherubini, A., Assogna, F., Piras, F., Quattrocchi, C., Peppe, A., Celsis, P., Rascol, O., Demonet, J.F., Stefani, A., Pierantozzi, M., Pontieri, F.E., Caltagirone, C., Spalletta, G., Sabatini, U., 2010. Magnetic resonance imaging markers of Parkinson's disease nigrostriatal signature. Brain 133, 3423–3433.
Pereira, J.B., Aarsland, D., Ginestet, C.E., Lebedev, A.V., Wahlund, L.O., Simmons, A., Volpe, G., Westman, E., 2015. Aberrant cerebral network topology and mild cognitive impairment in early Parkinson's disease. Hum. Brain Mapp. 36, 2980–2995.
Peterson, A.C., Li, C.R., 2018. Noradrenergic dysfunction in Alzheimer's and Parkinson's diseases-an overview of imaging studies. Front Aging Neurosci. 10, 127.
Peto, V., Jenkinson, C., Fitzpatrick, R., Greenhall, R., 1995. The development and validation of a short measure of functioning and well being for individuals with Parkinson's disease. Qual. Life Res. 4, 241–248.
Preacher, K.J., Hayes, A.F., 2004. SPSS and SAS procedures for estimating indirect effects in simple mediation models. Behav. Res. Methods Instrum Comput. 36, 717–731.
Preacher, K.J., Kelley, K., 2011. Effect size measures for mediation models: quantitative strategies for communicating indirect effects. Psychol. Methods 16, 93–115.
Pringsheim, T., Jette, N., Frolkis, A., Steeves, T.D., 2014. The prevalence of Parkinson's disease: a systematic review and meta-analysis. Mov Disord. 29, 1583–1590.
Rubinov, M., Sporns, O., 2010. Complex network measures of brain connectivity: uses and interpretations. Neuroimage 52, 1059–1069.
Schaefer, A., Kong, R., Gordon, E.M., Laumann, T.O., Zuo, X.N., Holmes, A.J., Eickhoff, S.B., Yeo, B., 2018. Local-global parcellation of the human cerebral cortex from intrinsic functional connectivity MRI. Cereb. Cortex 28, 3095–3114.
Shine, J.M., Aburn, M.J., Breakspear, M., Poldrack, R.A., 2018. The modulation of neural gain facilitates a transition between functional segregation and integration in the brain. Elife 7, e31130.
Shine, J.M., Bissett, P.G., Bell, P.T., Koyejo, O., Balsters, J.H., Gorgolewski, K.J., Moodie, C.A., Poldrack, R.A., 2016. The dynamics of functional brain networks: integrated network states during cognitive task performance. Neuron 92, 544–554.
Shine, J.M., Matar, E., Ward, P.B., Bolitho, S.J., Gilat, M., Pearson, M., Naismith, S.L., Lewis, S.J., 2013a. Exploring the cortical and subcortical functional magnetic resonance imaging changes associated with freezing in Parkinson's disease. Brain 136, 1204–1215.
Shine, J.M., Matar, E., Ward, P.B., Frank, M.J., Moustafa, A.A., Pearson, M., Naismith, S.L., Lewis, S.J., 2013b. Freezing of gait in Parkinson's disease is associated with functional decoupling between the cognitive control network and the basal ganglia. Brain 136, 3671–3681.
Skidmore, F., Korenkevych, D., Liu, Y., He, G., Bullmore, E., Pardalos, P.M., 2011. Connectivity brain networks based on wavelet correlation analysis in Parkinson fMRI data. Neurosci. Lett. 499, 47–51.
Sofic, E., Paulus, W., Jellinger, K., Riederer, P., Youdim, M.B., 1991. Selective increase of iron in substantia nigra zona compacta of parkinsonian brains. J. Neurochem. 56, 978–982.
Spillantini, M.G., Schmidt, M.L., Lee, V.M., Trojanowski, J.Q., Jakes, R., Goedert, M., 1997. Alpha-synuclein in Lewy bodies. Nature 388, 839–840.
Sporns, O., Tononi, G., Kotter, R., 2005. The human connectome: a structural description of the human brain. Plos Comput. Biol. 1, e42.
Suo, X., Lei, D., Li, N., Cheng, L., Chen, F., Wang, M., Kemp, G.J., Peng, R., Gong, Q., 2017. Functional brain connectome and its relation to Hoehn and Yahr stage in Parkinson disease. Radiology 285, 904–913.
Szewczyk-Krolikowski, K., Menke, R.A., Rolinski, M., Duff, E., Salimi-Khorshidi, G., Filippini, N., Zamboni, G., Hu, M.T., Mackay, C.E., 2014. Functional connectivity in the basal ganglia network differentiates PD patients from controls. Neurology 83, 208–214.
Wan, W., Jin, L., Wang, Z., Wang, L., Fei, G., Ye, F., Pan, X., Wang, C., Zhong, C., 2017. Iron deposition leads to neuronal alpha-synuclein pathology by inducing autophagy dysfunction. Front. Neurol. 8, 1.
Wang, C., Fan, G., Xu, K., Wang, S., 2013. Quantitative assessment of iron deposition in the midbrain using 3D-enhanced T2 star weighted angiography (ESWAN): a preliminary cross-sectional study of 20 Parkinson's disease patients. Magn. Reson. Imaging 31, 1068–1073.

Wang, J., Wang, X., Xia, M., Liao, X., Evans, A., He, Y., 2015. GRETNA: a graph theoretical network analysis toolbox for imaging connectomics. Front Hum. Neurosci. 9, 386.
Wang, Y., Liu, T., 2015. Quantitative susceptibility mapping (QSM): Decoding MRI data for a tissue magnetic biomarker. Magn. Reson. Med. 73, 82–101.
Ward, R.J., Zucca, F.A., Duyn, J.H., Crichton, R.R., Zecca, L., 2014. The role of iron in brain ageing and neurodegenerative disorders. Lancet Neurol. 13, 1045–1060.
Watts, D.J., Strogatz, S.H., 1998. Collective dynamics of 'small-world' networks. Nature 393, 440–442.
Wei, H., Dibb, R., Zhou, Y., Sun, Y., Xu, J., Wang, N., Liu, C., 2015. Streaking artifact reduction for quantitative susceptibility mapping of sources with large dynamic range. NMR Biomed. 28, 1294–1303.
Wei, H., Zhang, Y., Gibbs, E., Chen, N.K., Wang, N., Liu, C., 2017. Joint 2D and 3D phase processing for quantitative susceptibility mapping: application to 2D echo-planar imaging. NMR Biomed. 30.
Wen, M.C., Heng, H., Hsu, J.L., Xu, Z., Liew, G.M., Au, W.L., Chan, L.L., Tan, L., Tan, E.K., 2017. Structural connectome alterations in prodromal and de novo Parkinson's disease patients. Parkinsonism Relat. Disord. 45, 21–27.
Wu, B., Li, W., Guidon, A., Liu, C., 2012. Whole brain susceptibility mapping using compressed sensing. Magn. Reson. Med. 67, 137–147.
Xu, H., Wang, Y., Song, N., Wang, J., Jiang, H., Xie, J., 2017. New progress on the role of Glia in iron Metabolism and iron-induced degeneration of dopamine neurons in Parkinson's disease. Front. Mol. Neurosci. 10, 455.
Xu, X., Guan, X., Guo, T., Zeng, Q., Ye, R., Wang, J., Zhong, J., Xuan, M., Gu, Q., Huang, P., Pu, J., Zhang, B., Zhang, M., 2018. Brain atrophy and reorganization of structural network in Parkinson's disease with Hemiparkinsonism. Front. Human Neurosci. 12.
Xu, X., Wang, Q., Zhang, M., 2008. Age, gender, and hemispheric differences in iron deposition in the human brain: an in vivo MRI study. Neuroimage 40, 35–42.
Xuan, M., Guan, X., Gu, Q., Shen, Z., Yu, X., Qiu, T., Luo, X., Song, R., Jiaerken, Y., Xu, X., Huang, P., Luo, W., Zhang, M., 2017. Different iron deposition patterns in early- and middle-late-onset Parkinson's disease. Parkinsonism Relat. Disord. 44, 23–27.
Yan, C.G., Wang, X.D., Zuo, X.N., Zang, Y.F., 2016. DPABI: data processing & analysis for (Resting-State) brain imaging. Neuroinformatics 14, 339–351.
Zecca, L., Gallorini, M., Schunemann, V., Trautwein, A.X., Gerlach, M., Riederer, P., Vezzoni, P., Tampellini, D., 2001. Iron, neuromelanin and ferritin content in the substantia nigra of normal subjects at different ages: consequences for iron storage and neurodegenerative processes. J. Neurochem. 76, 1766–1773.
Zhang, M.Y., Katzman, R., Salmon, D., Jin, H., Cai, G.J., Wang, Z.Y., Qu, G.Y., Grant, I., Yu, E., Levy, P., Et, A., 1990. The prevalence of dementia and Alzheimer's disease in Shanghai, China: impact of age, gender, and education. Ann. Neurol. 27, 428–437.
Zhang, Y., Wei, H., Cronin, M.J., He, N., Yan, F., Liu, C., 2018. Longitudinal atlas for normative human brain development and aging over the lifespan using quantitative susceptibility mapping. Neuroimage 171, 176–189.
Zhong, S., He, Y., Shu, H., Gong, G., 2017. Developmental changes in topological asymmetry between hemispheric brain white matter networks from Adolescence to Young Adulthood. Cereb. Cortex 27, 2560–2570.